MRS Communications (2018), *8*, 289–296
© Materials Research Society, 2018
doi:10.1557/mrc.2018.56

MRS Communications

Research Letter

Alkyne-modified water-stable alkylammonium lead(II) iodide perovskite

Sayantan Sasmal and **Suresh Valiyaveettil,** Department of Chemistry, National University of Singapore, 3 Science Drive 3, Singapore 117543, Singapore; Materials Science Programme, Indian Institute of Technology Kanpur 208016, UP, India
Arun P. Upadhyay, Raj Ganesh S. Pala, and **Sri Sivakumar,** Department of Chemical Engineering, Materials Science Programme, Centre for Environmental Science & Engineering, Thematic Unit of Excellence on Soft Nanofabrication, Indian Institute of Technology Kanpur 208016, UP, India
Dharmadoss Sornadurai and **Chakram S. Sundar,** Materials Science Group, Indira Gandhi Centre for Atomic Research, Kalpakkam 603102, India

Address all correspondence to Raj Ganesh S. Pala, Sri Sivakumar and Suresh Valiyaveettil, **rpala@iitk.ac.in**; **srisiva@iitk.ac.in**; **chmsv@nus.edu.sg**

(Received 25 December 2017; accepted 27 March 2018)

Abstract

Perovskite materials are sensitive to environmental conditions. Here we report the synthesis and characterization of a hydrophobic alkylammonium lead(II) iodide perovskite with enhanced stability in water. Water stability was achieved by growing a shell of 4-[(N-3-butyne)carboxyamido]anilinium lead(II) iodide over methylammonium lead(II) iodide. As a proof of concept, the water-splitting reaction was performed using our new material coated on TiO_2, and a 7-fold increase in applied bias photon-to-current efficiency was observed as compared with standard p25-TiO_2. Such simple and versatile chemical modification to induce high water stability is useful toward exploring new applications for the perovskite materials.

Introduction

Organic–inorganic hybrid lead (II) halide perovskites attracted significant interests in photovoltaic devices owing to their easy accessibility, low defect density, excellent charge transport properties, and high-power conversion efficiency.[1–3] However, fast degradation of properties under the influence of environmental factors such as humidity,[4] light,[5] and heat[6] are some of the major obstacles toward commercialization of perovskite materials. Previous attempts to enhance the environmental stability that involve incorporation of pseudohalogens,[7] surface passivation with a capping agent,[8] and use of different methods of fabrication[9,10] were successful, but not enough to enhance the stability of hybrid perovskite for immersing in water, which is prerequisite for many electrochemical applications. One of the tried and tested methods to improve the stability and efficiency of perovskite materials include growing a shell of another semiconductor,[11] hydrophobic molecules[12] around the particles, to develop core–shell nanocrystals, or use of external passivating layers.[13,14] Recently, a few hydrophobic polymer coatings have been used to protect perovskite nanoparticles from the water.[15] Such coatings imposed an overwhelming electronic barrier on hybrid perovskite materials toward most photoelectrochemical (PEC) applications. In addition, these reported methods work well for solar cell application, but none of them is suitable as a universal method for stabilizing the perovskite nanocrystals inside water and perform the water-splitting reaction.

Here we report an in situ synthesis, characterization, and use of a hydrophobic shell of 4-[(N-3-butyne)carboxyamido]anilinium lead iodide ($NBCAnPbI_3$) to encapsulate $MAPbI_3$ perovskite crystals. The alkyne groups present in the shell induce sufficient hydrophobicity to prevent the diffusion of water from outside and protect $MAPbI_3$ crystals. This shell also possesses conduction band edge favorable for electron transfer from $MAPbI_3$ to outside electrodes, which is important to maintain the photosensitizing property of perovskite material. This unique combination of fascinating water stability and suitable band position make this assembly optimum for PEC reactions such as water splitting.

Experimental section

Full details of materials and methodologies are given in the Supplementary information.

Synthesis of $NBCAnPbI_3$ encapsulated $CH_3NH_3PbI_3$

First precursor solution was prepared by mixing of CH_3NH_3I (MAI, 0.196 g, 1.23 mmol), 4-carboxyanilinium iodide (CAnI, 0.326 g, 1.23 mmol), and PbI_2 (1.134 g, 2.46 mmol) in 2 ml of γ-butyrolactone at 60 °C for 12 h. 1-Amino-3-butyne (12.3 mmol) and the coupling agent 1-ethyl-3-(3-dimethylaminopropyl)carbodiimide (EDC, 5 mg, 0.026 mmol) were added to the above solution for full conversion of −COOH to −CO-NH− group. The solution was stirred at room temperature for 18 h for 3 days, with periodic monitoring. The precipitated solid was collected and heated at 85 °C for 20 h to remove the residual solvent. A gradual shift of color from yellow to brown was observed during the heating and the dry powder was used for further characterization. A similar procedure was adopted to make a control perovskite sample, $NBCAnPbI_3$ for comparison of properties.

https://doi.org/10.1557/mrc.2018.56 Published online by Cambridge University Press

Synthesis of 0.5 NBCAnPbI$_3${1 MAPbI$_3$}

This mixed perovskite was prepared by mixing CAnI and MAI in a ratio of 0.5:1 with stoichiometric amounts of PbI_2, followed by EDC-assisted alkyne functionalization, as described above.

Synthesis of MAPbI$_3$, CAnPbI$_3${MAPbI$_3$}, and TPbI$_3${MAPbI$_3$}

To prepare a control sample of pure $MAPbI_3$, a reported literature procedure was followed.[16] $CAnPbI_3\{CH_3NH_3PbI_3\}$ was prepared by heating the stoichiometric mixture of CAnI, MAI, and PbI_2 dissolved in γ-butyrolactone (2 mL) at 60 °C for 12 h at 80 °C till drying. *p*-Toluidinium lead (II) iodide ($TPbI_3$)-encapsulated $MAPbI_3$ ($TPbI_3\{MAPbI_3\}$) was prepared by mixing equimolar amounts of 4-toluidinium iodide (TI) and MAI along with the stoichiometric amounts of PbI_2 dissolved in γ-butyrolactone (2 mL) at 60 °C for 12 h. The precipitated solid was collected and heated at 80 °C to remove the excess solvent. The dry samples were used for further characterization.

Fabrication of photoanode

Fabrication of photoanode includes following steps: p25-TiO_2 paste (5 g, Degussa p25 powder) was prepared using the previously mentioned method.[17] A thin film of TiO_2 was cast over a cleaned ITO substrate (0.24 cm^2), followed by calcination at 450 °C for 30 min. A slurry of $NBCAnPbI_3\{MAPbI_3\}$ in γ-butyrolactone was spread over p25-TiO_2 film and heated at 85 °C for 20 h. In the third step, 0.1 g p25-TiO_2 paste (ethanol as solvent) was coated followed by heating at 85 °C for 60 min over $NBCAnPbI_3\{MAPbI_3\}$.

Results and discussion

The precursor solution was prepared by mixing MAI, CAnI, and PbI_2 in 2 mL of γ-butyrolactone, heated at 60 °C for 12 h. 1-Amino-3-butyne was then coupled in situ to a −COOH group of CAnI to get the final product. The procedure was demonstrated via a schematic diagram [Fig. 1(a)] and discussed in detail in the "Experimental" section.

Functionalization and proof of encapsulation

Successful alkyne functionalization via amide linkage between CAnI and 1-amino-3-butyne was demonstrated using Fourier-transform infrared spectroscopy (FTIR) spectra [Fig. 1(b)]. Amide-NH (~3352 cm^{-1}) and amide >C=O (~1620 cm^{-1}) along with terminal C≡C–H (~3253 cm^{-1}), C≡C (~2115 cm^{-1}) stretching frequencies in the spectrum of the product after functionalization confirms the alkyne group incorporation through acid–amine coupling reaction. The absence of broad −OH vibrations and shift of >C=O peak (from 1696 to 1620 cm^{-1}) in the IR spectra of the samples before and after functionalization showed the transformation of acid to amide groups in the final product. To prove the chemical formula of alkyne functionalized 4-carboxyanilinium lead iodide, same acid–amine coupling reaction was performed without adding MAI (see the Experimental section) and check with x-ray photoelectron spectroscopy (XPS). After successful alkyne functionalization [Fig. 1(c)], XPS survey scan performed at different regions of the sample revealed the presence of lead (Pb) and iodine (I) with an atomic ratio of 1:3 (Fig. S1). This 1:3 ratio of Pb:I along with successful alkyne functionalization indicates a possible molecular formula of our functionalized material as $NBCAnPbI_3$. The x-ray diffraction (XRD) pattern of $NBCAnPbI_3$ was indexed using TREOR software, which indicates an orthorhombic (*Pmmn*) crystal structure with lattice parameters, $a = 19.6442$, $b = 9.244$, and $c = 9.1901$. As we used MAI with a stoichiometric amount of PbI_2 along with the precursors of $NBCAnPbI_3$, the formation of a hybrid phase material $NBCAnPbI_3\{MAPbI_3\}$ is investigated using XRD. The powder XRD data [Fig. 1(d)] of the target material, $NBCAnPbI_3\{MAPbI_3\}$, were compared with homogeneous pure $MAPbI_3$ and $NBCAnPbI_3$ to identify the presence of both components in the final product. The presence of multiple diffraction peaks of $MAPbI_3$ in $NBCAnPbI_3\{MAPbI_3\}$ shown by a dotted line and * marks indicate the presence of $MAPbI_3$ in our target material $NBCAnPbI_3\{MAPbI_3\}$. Although some of the diffraction peaks of $MAPbI_3$ overlapped with the diffraction peaks of $NBCAnPbI_3$, the presence of two major diffraction peaks 110 and 220 (* marked) of $MAPbI_3$ in $NBCAnPbI_3\{MAPbI_3\}$ indicates the presence of tetragonal phase of $MAPbI_3$[18] in our target material $NBCAnPbI_3\{MAPbI_3\}$. The diffraction peaks of the most intense peaks (marked as +) corresponding to the (200) and (110) planes of $NBCAnPbI_3$ indicate the presence of $NBCAnPbI_3$ phases inside the hybrid material $NBCAnPbI_3\{MAPbI_3\}$. In addition, the hybrid materials prepared with a reduced molar ratio 1:0.5 for MAI:CAnI (see the Experimental section), followed by functionalization with 1-amino-3-butyne, led to the formation of both phases in the sample with reduced water stability. Moreover, UV–vis spectra of pure $MAPbI_3$ (Fig. S2, i) and $NBCAnPbI_3$ (Fig. S2, ii) were compared with $NBCAnPbI_3\{MAPbI_3\}$(Fig. S2, iii). The broad and strong absorption of $NBCAnPbI_3\{MAPbI_3\}$ (Fig. S2, iii) in the longer wavelength region indicate the presence of both $MAPbI_3$ and $NBCAnPbI_3$ in the material.

The formation of $NBCAnPbI_3$ shell over $MAPbI_3$ was investigated by transmission electron microscopy [TEM, Fig. 2(a)], which showed the presence of a well-connected network structure, instead of discrete particles. The presence of network structure implies an encapsulated architecture for the final materials, rather than the formation of a physical mixture of two different materials. Higher magnification image of the materials [Fig. 2(b)] indicates the presence of materials encapsulating discrete darker particles. High-resolution TEM micrograph of a dark spot [inset of Fig. 2(b)] shows lattice fringes with a *d*-value of ~0.278 nm, which matches with the (310) plane of tetragonal $MAPbI_3$[18] and brighter spot having a *d*-value of ~0.228 nm, which corresponds to the (104) plane of orthorhombic $NBCAnPbI_3$. No such encapsulating structure and the presence of discrete dark particles with 0.278 nm *d*-spacing were observed in the TEM micrographs of pure

https://doi.org/10.1557/mrc.2018.56 Published online by Cambridge University Press

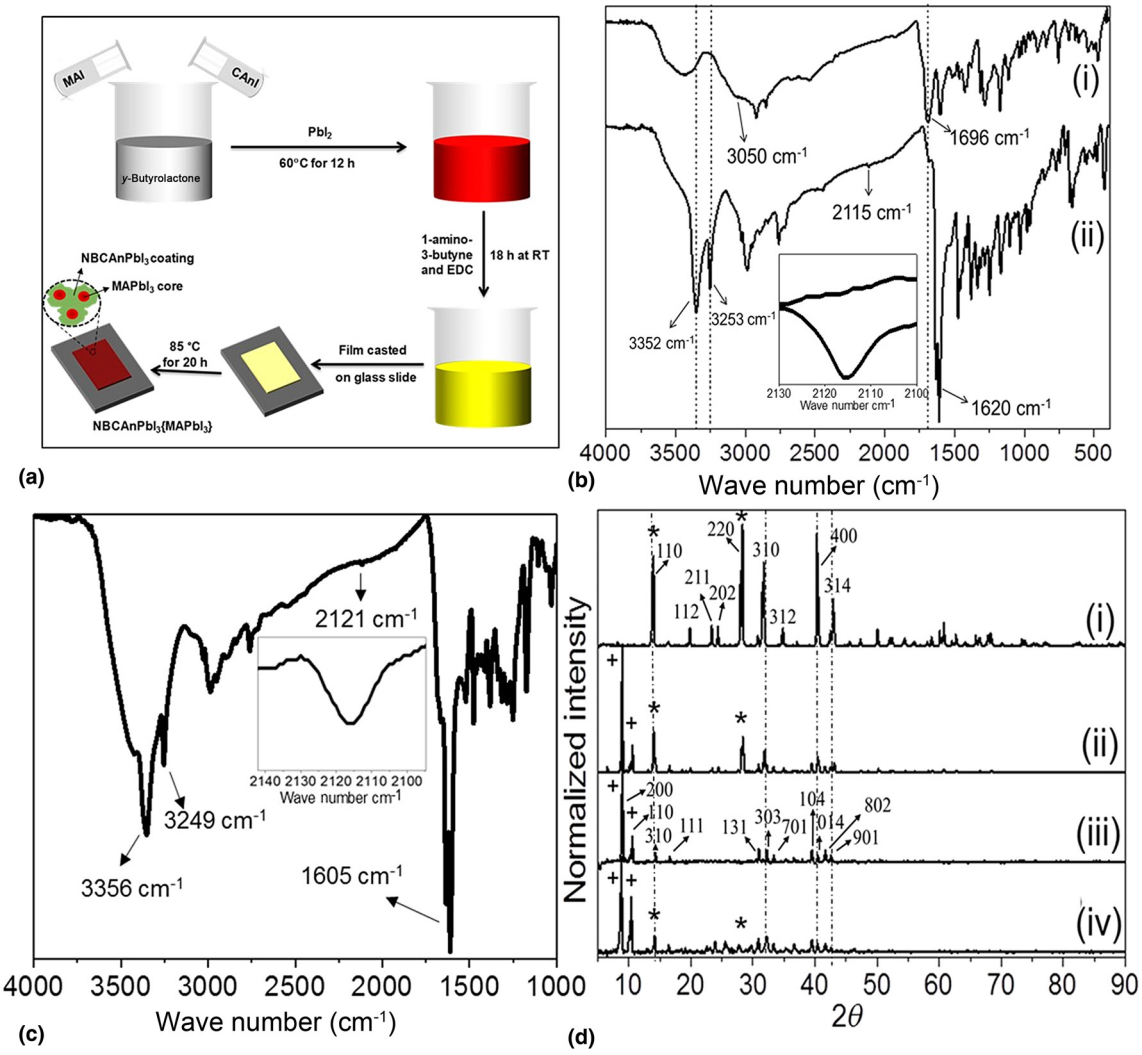


Figure 1. (a) Schematic representation of synthetic approach for the encapsulated $MAPbI_3$. (b) FTIR spectra of mixed perovskites before (i) and after (ii) amide linkage formation using EDC coupling. The inset shows the presence of C≡C stretching peak (~2115 cm^{-1}) of the spectrum. (c) FTIR spectra of pure $NBCAnPbI_3$. The inset shows the presence of C≡C stretching peak (~2121 cm^{-1}). (d) Powder XRD patterns of $MAPbI_3$ (i), $NBCAnPbI_3\{MAPbI_3\}$ (0.5:1) (ii), pure $NBCAnPbI_3$ (iii), $NBCAnPbI_3\{MAPbI_3\}$ (1:1) (iv), (+marks show two major peaks of $NBCAnPbI_3$. Dotted lines, specially the * mark, indicate the presence of $MAPbI_3$ in all samples except pure $NBCAnPbI_3$). The intensity of XRD peaks of $MAPbI_3$ gradually reduced with an increase in $NBCAnPbI_3$ amount in the mixed sample.

$MAPbI_3$ (Fig. S3). The control samples prepared using TI and CAnI using the same procedure (see the Experimental section) were also fully characterized and properties were compared. TEM micrographs of both $CAnPbI_3\{MAPbI_3\}$ [Fig. 2(c)] and $TPbI_3\{MAPbI_3\}$ [Fig. 2(d)] showed similar encapsulated structures with less extended architectures than the previously discussed $NBCAnPbI_3\{MAPbI_3\}$. This discrepancy in network structure formation could be attributed to different diffusion-limited aggregation (DLA) growth[19] in the presence of phenylammonium cations. The microstructure of the in situ generated bilayer is suggestive of classical DLA of $CAnPbI_3$ over $MAPbI_3$ [Fig. 2(c)] as well as $TPbI_3$ over $MAPbI_3$ [Fig. 2(d)]. Such a growth mechanism is prevalent in systems that have anisotropic diffusion coefficient of molecular species (in this case $CAnPbI_3$ and $TPbI_3$) due to structural heterogeneity (e.g., diffusion coefficient at a step-"edge" can be less than the diffusion coefficient on a "planar" step). This random walk of molecules and irreversible sticking to the perimeter of growing aggregates is already discussed in a previous literature.[20] The variation of sticking coefficient (K_{stick}) and change in cluster shape also explained earlier.[21] Also, lowering the value of K_{stick} affects the capture activity of branches of growing aggregates and channelize the diffusion toward center[21] to produce a network structure of $NBCAnPbI_3\{MAPbI_3\}$ shown in Figs. 2(a) and 2(b). To identify the presence of different phases in the control samples, we performed powder XRD analyses (Fig. S4)

https://doi.org/10.1557/mrc.2018.56 Published online by Cambridge University Press

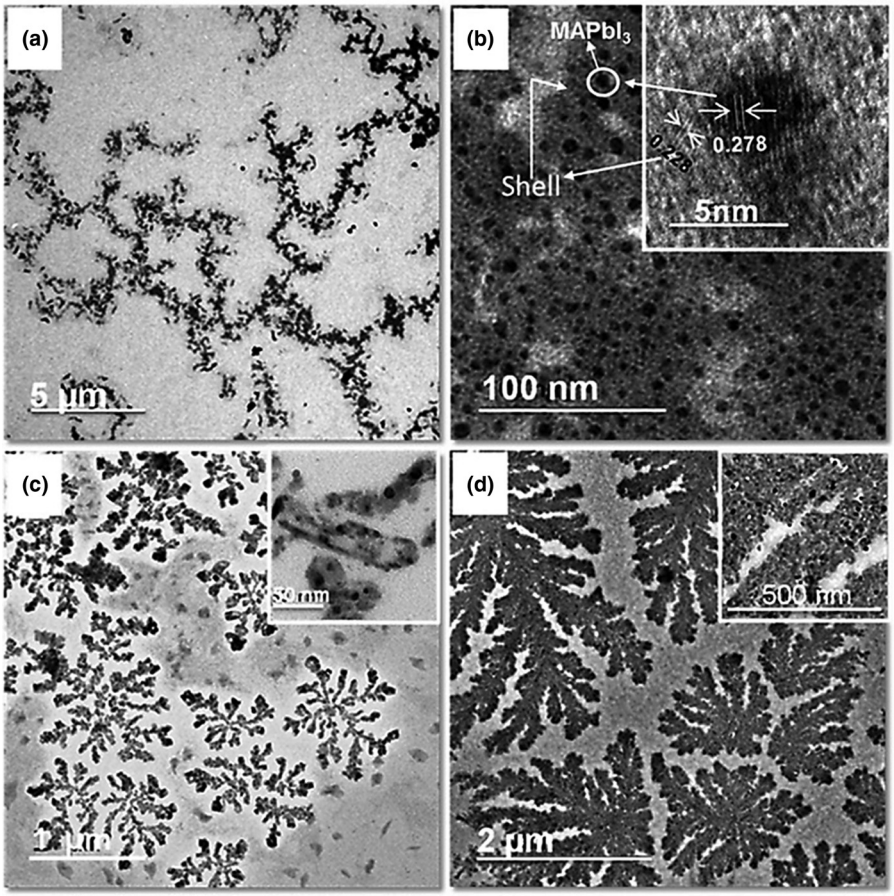


Figure 2. TEM micrographs of (a) network of NBCAnPbI$_3${MAPbI$_3$} and (b) magnified image of the network. The inset in (b) shows high-resolution micrograph where fringes of the dark spot with a *d*-spacing ~0.278 nm corresponding to the tetragonal MAPbI$_3$ and brighter region with a *d*-spacing ~0.228 nm corresponds to the shell of orthorhombic NBCAnPbI$_3$ (c) CAnPbI$_3${MAPbI$_3$} and (d) TPbI$_3${MAPbI$_3$} with their magnified images are shown in the inset.

of CAnPbI$_3${MAPbI$_3$} and TPbI$_3${MAPbI$_3$} perovskites. The peaks marked with a star in Fig. S4 indicate the presence of MAPbI$_3$ in both the materials. As expected, comparison of powder XRD data of pure CAnPbI$_3$ or TPbI$_3$ with mixed samples CAnPbI$_3${MAPbI$_3$} and TPbI$_3${MAPbI$_3$} showed the presence of phases corresponding to all components in the final samples (Fig. S4).

Investigation of water stability

Extended network formation observed for NBCAnPbI$_3${MAPbI$_3$} in TEM micrographs motivated us to investigate the water stability and compare with the established MAPbI$_3$ material. The black color of the material turns to yellow as soon as MAPbI$_3$ was immersed in water, which can also be monitored by UV–vis spectroscopy [Fig. 3(a)]. At the same time, no significant changes in colors were observed in the case of NBCAnPbI$_3${MAPbI$_3$} after immersing in water for 30 min [Fig. 3(b)], which indicates high water stability of the target hybrid material. The instability of conventional MAPbI$_3$ was further checked by dipping the film in water just for 30 s and monitored by XRD. The disappearance of all the characteristic diffraction peaks and appearance of completely new diffraction pattern shown in Fig. 3(c) proved that even 30 s of water immersion is sufficient to break tetragonal packing of MAPbI$_3$ led to the formation of PbI$_2$,[4] whereas minimum differences in powder XRD data before and after immersion in water for as long as 30 min [Fig. 3(d)] confirm the stability of NBCAnPbI$_3${MAPbI$_3$}. To check the moisture stability of the NBCAnPbI$_3${MAPbI$_3$}, the sample was kept inside a humidity chamber under 95% humidity for several days. Systematic XRD study of the test material exposed to moisture indicated no changes in the crystal structure (Fig. S5) within the first 10 days, which points to the high stability against moisture. The higher stability of the hybrid NBCAnPbI$_3${MAPbI$_3$} perovskite toward humidity and water is due to the hydrophobicity of the shell, which is confirmed by contact angle measurements. NBCAnPbI$_3${MAPbI$_3$} showed a higher contact angle [~104°, inset in Fig. 3(b)] as compared with hydrophilic MAPbI$_3$ (contact angle decreases quickly from 51° to 33° and stabilizes at 27°).[8] The instabilities of control samples, CAnPbI$_3${MAPbI$_3$} and

https://doi.org/10.1557/mrc.2018.56 Published online by Cambridge University Press

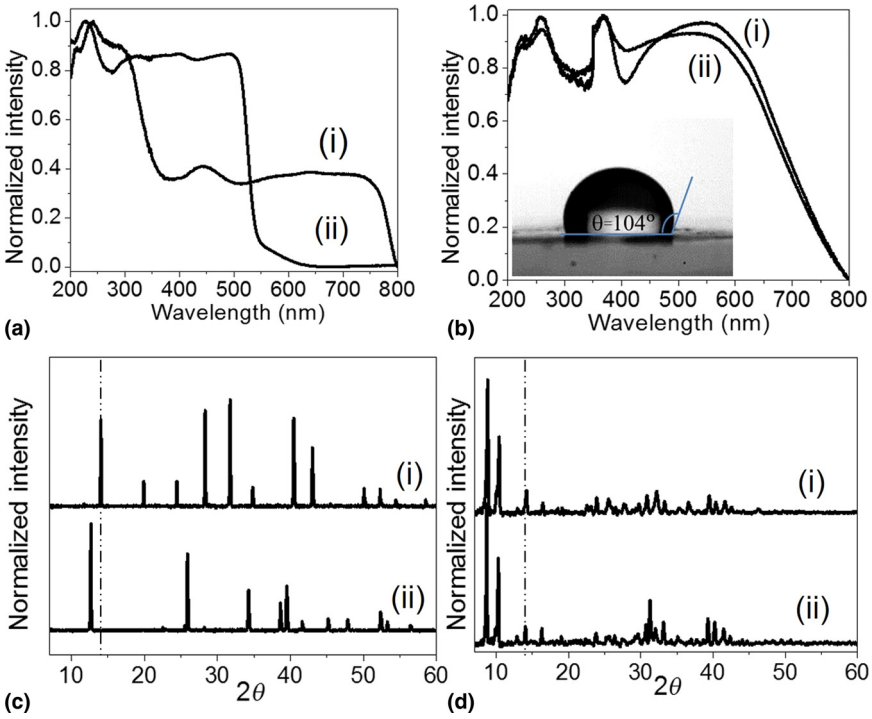


Figure 3. UV–vis spectra of $MAPbI_3$ (a) and $NBCAnPbI_3\{MAPbI_3\}$ (b) before (i) and after (ii) immersion in water. The inset shows the contact angle which was measured by placing a drop of water on top of the sample and recording the image using CCD camera. XRD spectra of $MAPbI_3$ (c) and $NBCAnPbI_3\{MAPbI_3\}$ (d) before (i) and after (ii) immersion in water. Dotted lines represent the (110) plane of conventional $MAPbI_3$ indicating the presence or absence of $MAPbI_3$ in the system.

$TPbI_3\{MAPbI_3\}$, in water indicate the importance of incorporation of hydrophobic alkyne functionalization.

Proof of concept demonstration of water splitting with high applied bias photon-to-current efficiency (ABPE)

Since $NBCAnPbI_3\{MAPbI_3\}$ is stable in water, the conduction band edge position of the shell material, $NBCAnPbI_3$, needs to be measured before performing an electrochemical reaction using the new mixed perovskite material. The standard electrochemical methods based on impedance spectroscopy and Mott–Schottky equation were used to calculate the flat band potential (see the Experimental section). $NBCAnPbI_3$-coated ITO was used as working electrode, Pt wire mesh, and Ag/AgCl electrode as a counter and reference electrodes, respectively. $K_3[Fe(CN)_6]$ (7×10^{-4} M) dissolved in 1 M KCl solution was used as electrolyte to record impedance spectra. Mott–Schottky plot was prepared using a previously published procedure.[22] The point of intersection is independent of frequencies applied, and the flat band potential of $NBCAnPbI_3$ calculated from intersection point is ~−0.6 V versus Ag/AgCl [−0.403 V versus normal hydrogen electrode (NHE)] [Fig. 4(a)]. The potential value conversion from NHE to vacuum was done by using conventional methods described in the literature.[23] The calculated conduction band of $NBCAnPbI_3$ is −4.1 eV close to the conduction band of TiO_2 and lower than that of $MAPbI_3$,[24] which enables the photogenerated electrons of $MAPbI_3$ to pass through the shell and available for electrochemical processes.

Favorable band position and water stability of $NBCAnPbI_3\{MAPbI_3\}$ imply the hybrid material to act as a sensitizer in the PEC application. As a proof of concept, the water-splitting reaction using the hybrid perovskite material as a sensitizer is demonstrated below. Details of photoanode fabrication are discussed in the Experimental section. A thin layer of commercial p25-TiO_2 was coated over $NBCAnPbI_3\{MAPbI_3\}$ to facilitate oxygen evolution reaction and to regenerate the $NBCAnPbI_3\{MAPbI_3\}$ by photogenerated electrons. The performance of fabricated heterostructures has been evaluated using a standard two probe method.[25] Under dark conditions, the thermodynamic requirement for water splitting is 1.23 V and a higher potential is required for effective water splitting due to overpotentials. However, in the presence of light, a good photosensitizer generates electrochemical bias from solar light such that the sum of the generated and applied electrochemical bias is >1.23 V. It is known that p25-TiO_2 is a mediocre PEC catalyst due to its high band gap,[26] which is unable to show major changes in current in the presence and absence of light. On the contrary, a significant increase in photocurrent in the presence of $NBCAnPbI_3\{MAPbI_3\}$-coated p25-TiO_2 was observed, which implies the sensitizing capability of mixed perovskite [Fig. 4(b)]. To further quantitatively

https://doi.org/10.1557/mrc.2018.56 Published online by Cambridge University Press

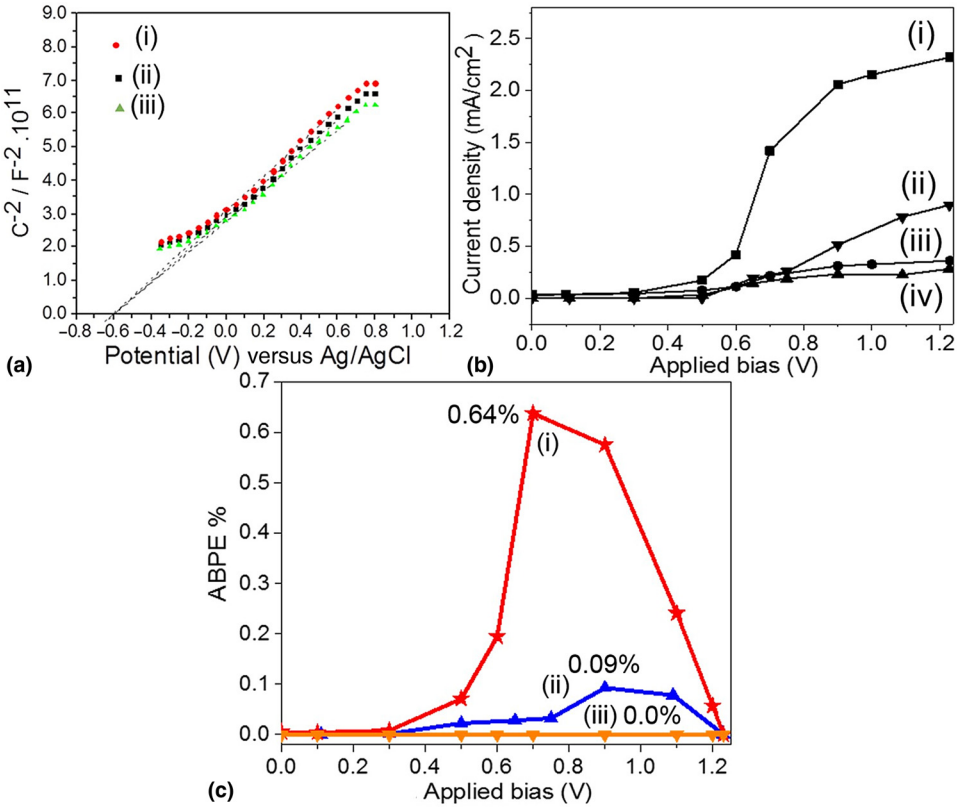


Figure 4. (a) Mott–Schottky plot for $NBCAnPbI_3$ measured at different frequencies (i) 1526 Hz, (ii) 954 Hz, (iii) 595 Hz, which indicates the flat band position at ~−0.6 V versus Ag/AgCl. (b) Two electrode analysis for photoelectrochemical water splitting using $NBCAnPbI_3\{MAPbI_3\}$ as a sensitizer (i = current under solar radiation, iii = dark current) and only with p25-TiO_2 (ii = current under solar radiation, iv = dark current). (c) Applied bias photo-to-current efficiency of p25-TiO_2 photoanode in the presence of $NBCAnPbI_3\{MAPbI_3\}$ (i), p25-TiO_2 only (ii), and in the presence of $NBCAnPbI_3$ (iii).

demonstrate the improved performance of photoanode, applied bias photon-to-current efficiency (ABPE) was evaluated using standard methods.[27] The ABPE efficiency was calculated to evaluate PEC cell performance under external potential using Eq. (1) given below.

$$\mathrm{ABPE} = \left[\frac{|j_{\mathrm{ph}}\,(\mathrm{mA\ cm^{-2}})| \times (1.23 - |V_{\mathrm{b}}|)\,(\mathrm{V})}{P_{\mathrm{total}}(\mathrm{mWcm^{-2}})}\right]_{\mathrm{AM1.5G}} \quad (1)$$

where j_{ph} is the photocurrent density, V_{b} is the applied bias between working and counter electrodes, and P_{total} is the incident illumination power density (AM1.5G, 100 $\mathrm{mW/cm^2}$). Since photocurrent achieved at low applied bias values play a significant role to understand the efficiency of a photoactive material, we have estimated the activity of the photoactive assembly by measuring applied bias between the counter and working electrodes below the thermodynamic potential of water (1.23 V), at which the maximum photon-to-current conversion is achieved.[28] ABPE of 0.64% was achieved by the photoanode in the presence of $NBCAnPbI_3\{MAPbI_3\}$ [Fig. 4(c, i)], whereas ABPE value drops to 0.09% in the absence of $NBCAnPbI_3\{MAPbI_3\}$ coating [Fig. 4(c, ii)]. A drastic improvement (~seven times) of ABPE in the presence of the hybrid perovskite indicates the important role of $NBCAnPbI_3\{MAPbI_3\}$ as a sensitizing material. Moreover, no such photoresponsive behavior was achieved without the presence of $MAPbI_3$ (presence of only shell $NBCAnPbI_3$), which is clearly represented by 0% ABPE shown in Fig. 4(c, iii), which unerringly proved the sensitizing role of $MAPbI_3$ to achieve high ABPE. We attribute this enhancement to much higher photon absorption and diffusion length of the $MAPbI_3$[4] core present in $NBCAnPbI_3\{MAPbI_3\}$. Facile e^-–h^+ pair separation is possible due to the favorable band position of $NBCAnPbI_3$, calculated using Mott–Schottky plot [Fig. 4 (a)] with respect to the band position of $MAPbI_3$ and TiO_2.[24] The calculated conduction band of $NBCAnPbI_3$ is −4.1 eV close to the conduction band of TiO_2 and lower than that of $MAPbI_3$,[24] which enable photogenerated electrons of $MAPbI_3$ to pass swiftly to TiO_2 electrode and allow $MAPbI_3$ to be regenerated by photogenerated electrons from p25-TiO_2 (Fig. S6). Both these effects are responsible for facile e^-–h^+ pair separation for PEC water splitting with ~seven times increment of ABPE value [Fig. 4(c)]. Gas evolved from anode during the electrochemical reaction was identified as oxygen and bubbles generated at Pt cathode as H_2, confirming the water-splitting reaction instead of any other reaction inside the

https://doi.org/10.1557/mrc.2018.56 Published online by Cambridge University Press

cell[29] (Fig. S7). It is also true that limited regeneration of $NBCAnPbI_3${$MAPbI_3$} by p25-TiO_2 is responsible for the slow oxygen evolution.[30] Such drawback can limit the photocurrent and reduces the life of the cell, as observed by the reduction in current density at a constant potential of 0.5 V (Fig. S8). This is corrected by adding methylene blue (MB) as a sacrificial agent.[31] Chronoamperometry measurements in the presence of MB showed a constant current density over a period of time as compared with the data collected without MB (Fig. S8). We are currently optimizing the performance of the materials and further investigation involving the fabrication of cells with good oxygen evolution properties.

Conclusion

In conclusion, we have deposited a hydrophobic shell of $NBCAnPbI_3$ over $MAPbI_3$ to enhance the stability in water under immersed condition. Alkyne functional groups play a crucial role toward introducing hydrophobicity with a large contact angle of ~104°. More importantly, suitable conduction band position of this crystalline network allows facile electron transfer from $MAPbI_3$ to TiO_2 and makes the whole assembly suitable for PEC applications. Interestingly, a 7-fold increase in ABPE value was observed than conventional p25-TiO_2 in the presence of $NBCAnPbI_3$-encapsulated $MAPbI_3$ as a sensitizer. We hope this study will open a new avenue of applications for perovskite materials in water splitting and photocatalytic hydrogen evolution, where immersion of electrodes in water is needed.

Supplementary material

The supplementary material for this article can be found at https://doi.org/10.1557/mrc.2018.56

Acknowledgments

The authors gratefully acknowledge the financial support from the Technology System Development program of the Department of Science and Technology, Government of India via project DST/TSG/SH/2011/106. S. S. and S. V. acknowledge the funding support from the National University of Singapore under the joint Ph.D. program between NUS and IITK. S. S. K. acknowledges the Centre for Environmental Science & Engineering, Thematic Unit of Excellence on Soft Nanofabrication, IITK.

References

1. A. Kojima, K. Teshima, Y. Shirai, and T. Miyasaka: Organometal halide perovskites as visible-light sensitizers for photovoltaic cells. *J. Am. Chem. Soc.* **131**, 6050 (2009).
2. M.M. Lee, J. Teuscher, T. Miyasaka, T.N. Murakami, and H.J. Snaith: Efficient hybrid solar cells based on meso-superstructured organometal halide perovskites. *Science* **338**, 643 (2012).
3. H. Zhou, Q. Chen, G. Li, S. Luo, T-B. Song, H-S. Duan, Z. Hong, J. You, Y. Liu, and Y. Yang: Interface engineering of highly efficient perovskite solar cells. *Science* **345**, 542 (2014).
4. J. Yang, B.D. Siempelkamp, D. Liu, and T.L. Kelly: Investigation of $CH_3NH_3PbI_3$ degradation rates and mechanisms in controlled humidity environments using in situ techniques. *ACS Nano* **9**, 1955 (2015).
5. D. Wang, M. Wright, N.K. Elumalai, and A. Uddin: Stability of perovskite solar cells. *Sol. Energy Mater. Sol. Cells* **147**, 255 (2016).
6. S. Kumar and A. Dhar: Accelerated thermal-aging-induced degradation of organometal triiodide perovskite on ZnO nanostructures and its effect on hybrid photovoltaic devices. *ACS Appl. Mater. Interfaces* **8**, 18309 (2016).
7. Q. Jiang, D. Rebollar, J. Gong, E.L. Piacentino, C. Zheng, and T. Xu: Pseudohalide-induced moisture tolerance in perovskite $CH_3NH_3Pb(SCN)_2I$ thin films. *Angew. Chem. Int. Ed.* **54**, 7617 (2015).
8. S. Yang, Y. Wang, P. Liu, Y.B. Cheng, H.J. Zhao, and H.G. Yang: Functionalization of perovskite thin films with moisture-tolerant molecules. *Nat. Energy* **1**, 15016 (2016).
9. G. Niu, W. Li, F. Meng, L. Wang, H. Donga, and Y. Qiu: Study on the stability of $CH_3NH_3PbI_3$ films and the effect of post-modification by aluminum oxide in all-solid-state hybrid solar cells. *J. Mater. Chem. A* **2**, 705 (2014).
10. L. Zheng, Y.H. Chung, Y. Ma, L. Zhang, L. Xiao, Z. Chen, S. Wang, B. Qu, and Q. Gong: A hydrophobic hole transporting oligothiophene for planar perovskite solar cells with improved stability. *Chem. Commun.* **50**, 11196 (2014).
11. P. Da, M. Cha, L. Sun, Y. Wu, Z-S. Wang, and G. Zheng: High-performance perovskite photoanode enabled by Ni passivation and catalysis. *Nano Lett.* **15**, 3452 (2015).
12. J.H. Kim, Y. Jo, J.H. Kim, J.W. Jang, H.J. Kang, Y.H. Lee, D.S. Kim, Y. Jun, and J.S. Lee: Wireless solar water splitting device with robust cobalt-catalyzed, dual-doped $BiVO_4$ photoanode and perovskite solar cell in Tandem: a dual absorber artificial leaf. *ACS Nano* **9**, 11820 (2015).
13. D.N. Dirin, S. Dreyfuss, M.I. Bodnarchuk, G. Nedelcu, P. Papagiorgis, G. Itskos, and M.V. Kovalenko: Lead halide perovskites and other metal halide complexes as inorganic capping ligands for colloidal nanocrystals. *J. Am. Chem. Soc.* **136**, 6550 (2014).
14. I. Hwang, I. Jeong, J. Lee, M.J. Ko, and K. Yong: Enhancing stability of perovskite solar cells to moisture by the facile hydrophobic passivation. *ACS Appl. Mater. Interfaces* **7**, 17330 (2015).
15. S. Guarnera, A. Abate, W. Zhang, J.M. Foster, G. Richardson, A. Petrozza, and H.J. Snaith: Improving the long-term stability of perovskite solar cells with a porous Al_2O_3 buffer layer. *J. Phys. Chem. Lett.* **6**, 432 (2015).
16. H-S. Kim, C-R. Lee, J-H. Im, K-B. Lee, T. Moehl, A. Marchioro, S-J. Moon, R. Humphry-Baker, J-H. Yum, J.E. Moser, M. Grätzel, and N-G. Park: Lead iodide perovskite sensitized all-solid-state submicron thin film mesoscopic solar cell with efficiency exceeding 9%. *Sci. Rep.* **2**, 591 (2012).
17. S. Ito, P. Chen, P. Comte, M.K. Nazeeruddin, P. Liska, P. Pechy, and M. Grätzel: Fabrication of screen-printing pastes from TiO2 powders for dye-sensitised solar cells. *Prog. Photovolt.: Res. Appl.* **15**, 603 (2007).
18. T. Oku: Crystal Structures of CH3NH3PbI3 and Related Perovskite Compounds Used for Solar Cells, Solar Cells-New Approaches and Reviews, ed. L.A. Kosyachenko, InTech, Rijeka, Croatia ISBN: 78-953-51-2184-8, DOI: 10.5772/59284. (2015). Available at: http://www.intechopen.com/books/solar-cells-new-approaches-and-reviews/crystal-structures-of-ch3nh3pbi3-and-related-perovskite-compounds-used-for-solar-cells.
19. F. Maxim, P. Ferreira, P.M. Vilarinho, and I. Reaney: Hydrothermal synthesis and crystal growth studies of $BaTiO_3$ using Ti nanotube precursors. *Cryst. Growth Des.* **8**, 3309 (2008).
20. H. Brune, C. Romainczyk, H. Roder, and K. Kern: mechanism of the transition from fractal to dendritic growth of surface aggregates. *Nature* **369**, 469 (1994).
21. B. Ranguelov, D. Goranova, V. Tonchev, and R. Yakimova: Diffusion limited aggregation with modified local rules. *C. R. Acad. Bulg. Sci.* **65**, 913 (2012).
22. K. Gelderman, L. Lee, and S.W. Donne: Flat-band potential of a semiconductor: W using the Mott–Schottky equation. *J. Chem. Educ.* **84**, 685 (2007).
23. M. Grätzel: Photoelectrochemical cells. *Nature* **414**, 338 (2001).
24. S. Aharon, A. Dymshits, A. Rotem, and L. Edgar: Temperature dependence of hole conductor free formamidinium lead iodide perovskite based solar cells. *J. Mater. Chem. A* **3**, 9171 (2015).
25. T. Hisatomi, J. Kubota, and K. Domen: Recent advances in semiconductors for photocatalytic and photoelectrochemical water splitting. *Chem. Soc. Rev.* **43**, 7520 (2014).
26. R. Daghrir, P. Drogui, and D. Rober: Modified TiO_2 for environmental photocatalytic applications: a review. *Ind. Eng. Chem. Res.* **52**, 3581 (2013).

https://doi.org/10.1557/mrc.2018.56 Published online by Cambridge University Press

27. Z. Chen, T.F. Jaramillo, T.G. Deutsch, A. Kleiman-Shwarsctein, A. J. Forman, N. Gaillard, R. Garland, K. Takanabe, C. Heske, M. Sunkara, E.W. McFarland, K. Domen, E.L. Miller, J.A. Turner, and H.N. Dinh: Accelerating materials development for photoelectrochemical hydrogen production: standards for methods, definitions, and reporting protocols. *J. Mater. Res.* **25**, 3 (2010).
28. A.P. Upadhyay, D.K. Behara, G.P. Sharma, M. Gyanprakash, R.G.S. Pala, and S. Sivakumar: Fabricating appropriate band-edge-staggered hetero-semiconductors with optically activated Au nanoparticles via click chemistry for photoelectrochemical water splitting. *ACS Sustain. Chem. Eng.* **4**, 4511 (2016).
29. Y. Gao, X. Ding, J. Liu, L. Wang, Z. Lu, L. Li, and L. Sun: Visible light driven water splitting in a molecular device with unprecedentedly high photocurrent density. *J. Am. Chem. Soc.* **135**, 4219 (2013).
30. J. Wang, H.X. Zhong, Y.L. Qin, and X.B. Zhang: An efficient three-dimensional oxygen evolution electrode. *Angew. Chem. Int. Ed.* **52**, 5248 (2013).
31. K.H. Ji, D.M. Jang, Y.J. Cho, Y. Myung, H.S. Kim, Y. Kim, and J. Park: Comparative photocatalytic ability of nanocrystal-carbon nanotube and -TiO_2 nanocrystal hybrid nanostructures. *J. Phys. Chem. C* **113**, 19966 (2009).

https://doi.org/10.1557/mrc.2018.56 Published online by Cambridge University Press